Title: "Mismatch Repair-Proficient Colorectal Cancer can evade Immune Surveillance Through an Intrinsic Suppressive Program"

Chiara Maria Cattaneo [1,*,#], Sharon Scardellato [2,3*], Gianluca Mauri [4], Vittoria Matafora [2], Veera Ojala [2], Costanza Cannariato [5], Rosaria Chilà [2], Zulma Irene Magnani [5], Wouter Scheper [6], Luca Lazzari [2], Emile E. Voest [6,7], Maria Chiara Bonini [5], Angela Bachi [2], Salvatore Siena [4,8], Silvia Marsoni [2], Giovanni Germano [2,9], Alberto Bardelli [2,10,#]

[1] IRCCS Humanitas Research Hospital, via Manzoni 56, 20089 Rozzano, Milan, Italy

[2] IFOM ETS – The AIRC Institute of Molecular Oncology, 20139 Milan, Italy.

[3] *Current affiliation:* Department of Cell Biology-Inspired Tissue Engineering, MERLN Institute for Technology-Inspired Regenerative Medicine, Maastricht University, the Netherlands.

[4] Department of Hematology, Oncology, and Molecular Medicine, Grande Ospedale Metropolitano Niguarda, Milan, Italy

[5] Division of Immunology, Transplantation and Infectious Diseases, San Raffaele Scientific Institute, 20132 Milan, Italy.

[6] Department of Molecular Oncology and Immunology, the Netherlands Cancer Institute, Amsterdam, The Netherlands

[7] Oncode Institute, Utrecht, The Netherlands

[8] Department of Oncology and Hemato-Oncology, University of Milan, 20162 Milan, Italy

[9] Department of Medical Biotechnology and Translational Medicine, University of Milano, 20054 Milan, Italy.

[10] Department of Oncology, Molecular Biotechnology Center, University of Torino, 10126 Torino, Italy.

* Authors equally contributed

Corresponding authors

Running Title: "Intrinsic Suppression Drives Immune Evasion in MMRp-CRC"

Correspondence to:

Prof. Alberto Bardelli:

IFOM, Istituto Fondazione di Oncologia Molecolare ETS.

Address: via Adamello 16, Milano, 20139, Italy.

Phone: +39-011-9933235.

Email: alberto.bardelli@unito.it

Chiara M. Cattaneo, PhD

IRCCS Humanitas Research Hospital

Address: via Rita levi Montacini, 4, 20072 Pieve Emanuele (MI)

Phone: +39 02 8224 5234

Email: chiara.cattaneo@humanitasresearch.it

Declaration of interests

S.Si. is an advisory board member for Agenus, AstraZeneca, Bayer, BMS, CheckmAb, Daiichi-Sankyo, Guardant Health, Merck, Novartis, Roche-Genentech, and Seagen. G.G. is a stock shareholder of NeoPhore. A.B. received research support from NeoPhore. A.B. is a stock shareholder of NeoPhore and Kither Biotech. A.B. is a scientific advisory board member for NeoPhore. No other disclosures were reported.

Abstract

While microsatellite-instable (MSI) colorectal cancers (CRC), reflecting mismatch repair deficiency, often respond to immune checkpoint inhibitors, microsatellite-stable (MSS) tumors remain largely resistant. This disparity is typically attributed to differences in neoantigen load. However, whether antigen-independent mechanisms contribute to immune evasion in MSS-CRC remains unclear. To address this, we engineered a model in which MSI- and MSS-CRC cells express identical levels of a defined antigen recognized by TCR-engineered T cells. Despite equivalent antigen presentation, MSS tumors exhibited impaired T-cell activation, reduced cytotoxicity, and resistance to killing. We linked this immune evasion to the MSS tumor secretome, which suppressed immune responses even in immunogenic MSI cells by impairing immune synapse formation. Surfaceome profiling by mass spectrometry identified glycosylation-dependent alterations that impair immune recognition. Our findings demonstrate that MSS-CRC evades immune attack via intrinsic secretome-driven mechanisms, independent of antigenicity. Targeting glycosylation-linked suppressive pathways may restore T-cell responsiveness and improve immunotherapy efficacy in MSS-CRC.

Statement of significance

This study reveals that mismatch repair-proficient colorectal cancers resist T-cell attack not only due to low neoantigen load but also through glycosylation-dependent, secretome-mediated immune suppression. These findings uncover a previously unrecognized immune evasion mechanism and identify actionable pathways to restore immunotherapy responsiveness in resistant colorectal tumors.

Introduction

Colorectal cancers (CRCs) can be classified based on the functional status of the DNA mismatch repair system (MMR) into two main subtypes: MMR-proficient (MMRp) and MMR-deficient (MMRd) tumors (1). In MMRd CRCs, the inactivation of the MMR machinery is most commonly due to genetic or epigenetic alterations causing loss of function of the *MLH1*, *MSH2*, *MSH6* and *PMS2* genes. This leads to genetic hypermutability and the accumulation of insertion-deletion mutations at microsatellite loci, a phenomenon known as microsatellite instability (MSI) (2). In colorectal cancer, MSI is therefore considered a hallmark feature of MMR deficiency. Conversely, MMRp tumors retain an intact MMR system and are characterized by microsatellite stability (MSS). MMRp/MSS tumors dominate the CRC landscape, representing approximately 85% of primary CRC cases. When considering the metastatic setting, their prevalence is even higher, accounting for nearly 95% of CRC patients (3). For clarity and consistency with experimental readouts throughout this study, tumors are hereafter referred to according to their microsatellite status as MSI or MSS.

The advent of cancer immunotherapy, in particular the use of checkpoint inhibitors targeting the programmed cell death protein 1 (PD-1) and the cytotoxic T-lymphocyte associated protein 4 (CTLA-4), has shown impressive clinical results in a subset of patients with solid tumors (4). Patients affected by metastatic MSI-CRC often respond to therapies based on immune checkpoint blockade (ICB), while those with MSS tumors do not (5).

MSI tumors usually display high tumor mutational burden (TMB), a feature linked to rapid progression but also to favorable prognosis in CRC (6). Because of their high mutational burden, MSI tumors express a high number of neoantigens, novel protein sequences resulting from tumor-specific mutations that, when expressed on MHC class I or II molecules, may be recognized by patient T cells. According to the prevalent view, high TMB leading to elevated number of neoantigens increases tumor's visibility to the T cell-based immune system (7). Levels of TMB are correlated with therapeutic response to ICB and, as a result, the U.S. Food and Drug Administration (FDA) has granted tumor-agnostic approval for treatment with anti-PD-1 pembrolizumab for adult and pediatric patients with unresectable or metastatic solid tumors exhibiting a TMB higher than 10 mut/Mb (8,9). Therapies based on checkpoint inhibitors are emerging as the standard of care treatment for MSI CRCs (10,11,12,13,14,15).

With the exception of specific cases (e.g. POLE-mutated tumors), MSS tumors are instead characterized by a much lower number of mutations and the prevalent view functionally links this feature to ineffective immunogenicity and lack of response to ICI (3). However, recent insights suggest a more nuanced picture. For instance, upon administering immunotherapy, MSS tumors show markers of immune activation, such as surge in $CD8^+$ T cells or heightened IFNγ score, albeit with minimal (or absent) tumor regression (11). Moreover, with the goal of increasing the immunogenicity of MSS tumors, innovative clinical strategies have been implemented. For example, the alkylating agent temozolomide (TMZ) has been used to induce a "hypermutant" status in MSS patients, as a priming treatment to boost the number of tumor's neoantigens, prior to anti-PD1 treatment (16,17,18). Yet, despite an increase of the TMB, only a subset of patients benefited from ICB, while the majority of the patients remained refractory to checkpoint inhibition. These results suggest that factors beyond neoantigen load may be involved in therapeutic resistance of MSS tumors to cancer immunotherapies (19). It is conceivable that during their development, CRC could have acquired active mechanisms to evade immune surveillance.

Elucidating the mechanisms behind the poor response of MSS tumors is key to develop new therapeutic strategies. However, the complexity of the tumor-immune system interaction, consisting of many different intrinsic and extrinsic effectors, makes it difficult to functionally pinpoint the underlying mechanism(s) of resistance (20). To tackle this issue, we developed a model system

whereby both MSI and MSS tumor cells express equal levels of a given antigen which is recognized by engineered T cells. Using this model, we tested the hypothesis that the lack of T cell-mediated tumor recognition that characterizes MSS CRC might be due to an intrinsic resistance to T cell attack, and not only due to the low mutational burden.

Results

To test the potential impact of intrinsic characteristics of MSS tumors on immune system recognition, we developed a tightly controlled experimental platform (Figure 1A). To ensure unbiased assessment, it was necessary to keep the tumor recognition conditions identical across all samples. To achieve this, peripheral blood mononuclear cells (PBMCs) were isolated from a healthy donor, followed by sorting and transduction of the $CD8^+$ T cells fraction with a T cell receptor (TCR) of known specificity. This preparation assures consistent and reproducible recognition across all experiments. In parallel, patient-derived tumor organoids (PDOs) from both MSI and MSS CRC tumors were established and screened for expression of a specific MHC-class-I molecule, HLA-A2. This step ensured that an identical antigen of choice could be uniformly presented to the previously engineered T cells, allowing for a controlled comparison between MSI and MSS tumor recognition.

We successfully established and cultured human tumor organoids from surgical specimen obtained from a cohort of 32 patients with either MSI (n=6) or MSS (n=26) CRC tumors (Table 1). Immunohistochemistry assessments confirmed the MMRd/MSI or MMRp/MSS profile of these organoids, based on the detection of MLH1, MSH2, MSH6 and PMS2 expression, as shown in Supplementary Figure 1. Tumor organoids screening for MHC expression revealed variable levels of surface expression of MHC class-I and class-II molecules (Supplementary Figure 2A-B). The evaluation was conducted both with and without pre-stimulation using IFNγ. The presence of the primary HLA allele of interest, HLA-A2, was tested and detected in 12 different PDOs (Supplementary Figure 2C). Furthermore, we checked Programmed Cell Death Ligand 1 (PD-L1) expression levels upon IFNγ stimulation (Supplementary Figure 3), to determine whether the addition of immune checkpoint inhibitors in subsequent experiments would be required.

In parallel, we isolated $CD8^+$ T cells from healthy donor PBMCs, and retrotransduced them with the 1D3-TCR ($MART1_{25-35}$-specific) antigen (Supplementary Figure 4A) (21). After antibiotic selection and expansion, we tested antigen-specific activation capabilities by evaluating the number of CD137 expressing T cells in the presence (or not) of the target antigen Mart-1_{ELA} (Supplementary Figure 4B). Additionally, we confirmed the competence of T cells to react in the presence of the 12 HLA-$A2^+$ PDOs (4 MSI and 8 MSS), when loaded with different concentrations of the Mart-1_{ELA} antigen, the MHC-affinity enhanced version of Mart-1_{25-35}, which is specifically recognized by the transgenic TCR. T cell

activation was evaluated by measuring surface expression of CD137 and release of IFNγ (Supplementary Figure 5 and Supplementary Figure 6, respectively).

To distinguish between the MSI and MSS tumors' intrinsic capabilities of being recognized by the immune system, we selected organoids with comparable HLA-A2 expression levels and engineered them to present the same target antigen (MART-1_{ELA}) (Figure 1B). Engineering of PDOs was obtained via peptide loading with a concentration of 0.02 μM of MART-1_{ELA} antigen, thus preventing saturation across all samples. This decision was supported by the findings presented in Supplementary Figure 5 and 6, where saturation was reached with 0.1 μM of MART-1ELA in several samples (MSS_16, MSS_17, MSS_21, MSS_22, MSS_24, MSS_25 in Supplementary figure 5; MSI_03 and MSS_22 in Supplementary Figure 6). Notably, when T cells were placed in the presence of MSI tumors, they secreted similar amount of IFNγ. However, when the same T cells were exposed to MSS tumors, there was a consistent 60-85% reduction in IFNγ secretion (Figure 1C). Similar secretion patterns were observed for other effector molecules, such as tumor necrosis factor-α (TNFα) (Figure 1D and Supplementary Figure 7A), Granzyme A (Figure 1E and Supplementary Figure 7B) and Granzyme B (Figure 1F and Supplementary Figure 7C). T cell reactivity assessed by CD137 expression led to analogous results. In the presence of MSI tumors, TCR-transduced T cells showed comparable levels of CD137 expression. However, in the majority of the MSS PDOs, exposure to T cells led to a significantly diminished reactivity level (Figure 1G-H). These observations held true also when the wildtype, non-MHC-affinity enhanced, variant MART-1_{EEA} was used (Supplementary Figure 8A-B).

Next, a 24-hour killing coculture assay (22,23) was used to assess how effectively the different patient-derived tumor organoids were eliminated by T cells. Both FarRed signaling and flow cytometry-based quantifications were used to assess the amount of surviving tumor cells. As shown in Figure 1I-J, MSI PDOs showed a notable reduction of the count of live cells (~50%) compared to controls, whereas MSS PDOs remained largely unaffected, with no killing detected (Figure 1I-J).

We reasoned that these results pointed to the existence of mechanisms which extend beyond mere mutational (neo)antigenic burdens, limiting response of MSS CRC to ICB.

To explore the immunomodulatory milieu during antigen recognition, we profiled the supernatants from MSI and MSS tumor organoids, each loaded with the MART-1_{ELA} peptide and co-cultured with autologous T cells, using a 96-plex Immuno-Oncology panel (24) (Figure 2A; Supplementary Figure 9). Comparison of MSI versus MSS co-cultures revealed multiple statistically significant differences in protein abundance. In particular, hallmark effector cytokines of T cell activation, including IFN-γ and TNF-α, were markedly elevated in the presence of MSI organoids, and a distinct array of chemokines and inflammatory mediators involved in immune cell recruitment and

intercellular communication were differentially expressed - findings that agree with our earlier functional assays. Strikingly, further inspection of the significant hits revealed that several mediators were not solely T cell-derived but were also secreted by the tumor organoids themselves (Figure 2A).

This dual origin suggests the existence of tumor-intrinsic circuits that may contribute to the immune modulatory phenotype we observe. We therefore hypothesized that tumor-secreted factors play a direct role in shaping the secretome and may constitute an alternative mechanism of immune resistance in our system.

To investigate whether factors secreted by CRC cells (the secretome) played a role in restricting their recognition by T cells, we utilized conditioned media (CM) from MSI and MSS PDOs, collected 24 hours after IFNγ stimulation (Figure 2B). We set up a T cell recognition assay which involved measuring intracellular IFNγ expression levels upon coculture with MSI tumor cells, in the presence of PDO-derived conditioned media. MSI tumor cell recognition was not affected by conditioned media derived from MSI tumor organoids. Strikingly, when MSS-derived conditioned media was used, T cell recognition of MSI tumor cells was markedly impaired (> 50% reduction) in all cases (Figure 2C-D). The killing efficacy of T cells was similarly impaired in the same experimental conditions (Figure 2E-F).

To further delve into the functional mechanisms constraining T cell functionality, we evaluated the impact of PDO-derived conditioned media on T cells by examining three key parameters: viability, proliferation, and target recognition capability. T cell viability was determined using an ATP release assay. Following 24 hours of culture in the presence of different conditioned media, no significant alterations in T cells viability were observed (Supplementary Figure 10A). Next, T cell proliferation, both unstimulated and stimulated by the Mart-1_{ELA} antigen, was measured using flow cytometry. The presence of conditioned media from MSS tumor organoids did not significantly affect T cell proliferation (Supplementary Figure 10B). Finally, to assess T cell target recognition, we utilized professional antigen-presenting cells (APCs) loaded with the Mart-1_{ELA} peptide. T cells were cocultured for 5 hours with the APCs in the presence of different conditioned media, and intracellular IFNγ expression was measured. Consistently with previous data, no significant differences were observed across the different conditioned media used (Supplementary Figure 10C).

These results show that the conditioned media derived from MSI and MSS co-cultures had no detectable impact on T cell viability, proliferation, or activation, indicating the absence of a direct suppressive effect on T cell functionality. Notably, professional APCs loaded with the same MART-1_{ELA} peptide were efficiently recognized by T cells even in the presence of tumor-derived conditioned media. These findings suggest that the impaired recognition observed in tumor organoid–T cell co-

cultures is not due to a general inhibition of T cell responsiveness, but rather reflects a mechanism that specifically interferes with T cell–tumor cell interactions.

Given that the observed impairment was specific to tumor–T cell interactions, we next sought to functionally assess the quality of this interaction under different conditions. Specifically, we focused on two parameters: the degree of T cell engagement, and the strength of the resulting interactions, reflecting the stability and avidity of T cell–tumor contacts. These metrics allowed us to quantitatively evaluate how conditioned media influences the formation and robustness of the tumor–T cell binding.

To quantify T cell engagement with tumor cells, we performed high-content microscopy on co-cultures of labeled T cells and tumor organoids. The proportion of T cells in direct contact with tumor cells was calculated and used as a measure of engagement efficiency across conditions (Figure 3A). First, to assess whether tumor-intrinsic properties influence the ability of T cells to establish contact, independently of antigen presentation, we used this assay to compare T cell engagement across different MSI and MSS tumor organoids, all presenting the MART-1_{ELA} antigen (Figure 3B). Next, to isolate the impact of MSS tumor-derived secretome on the physical interaction between T cells and tumor cells, we focused on two different MSI tumors singularly and evaluated engagement in the presence of different conditioned media (Figure 3C). These experiments revealed that T cell engagement varies significantly between MSI and MSS tumor organoids, despite presentation of the same cognate antigen. For MSI tumors, we observe that approximately 60% of T cells established contact with tumor cells, whereas with MSS tumors engagement dropped to as low as 20% (Figure 3B). A similar reduction in engagement was seen when MSI tumor organoids were placed with T cells in the presence of MSS-derived conditioned media, resulting in a decrease of approximately 50% in the proportion of engaged T cells (Figure 3C).

To complement our engagement analysis, we next assessed the strength of T cell–tumor interactions using a single-cell force-based assay (25). This approach revealed marked differences in the stability of T cell-tumor contacts between MSI and MSS tumors, mirroring what we assessed with the engagement data (Figure 3D). Notably, when the binding strength to MSI tumors was measured in the presence of MSS derived conditioned media, we noticed a significant reduction (Supplementary Figure 10D).

These findings suggest that MSS tumor-derived soluble mediators can modulate the efficiency of T cell–tumor interactions, impairing the quality of the immune synapse.

To understand the mechanisms behind our observation, we first analyzed the surface expression of four key molecules critical to our system. We exposed four different MSI tumor organoids to conditioned media collected from both MSI and MSS tumor organoids. Following this exposure, we assessed the surface expression levels of MHC-I, HLA-A2, MHC-II, and PDL-1. No significant differences were observed in the expression of these molecules across the different conditioned media treatments (Supplementary Figure 10E).

We next sought an unbiased view of how tumor-derived secretomes remodel the tumor cell surface. To this end, we performed mass spectrometry–based membrane proteome on MSI tumor organoids that had been pre-activated with IFN-γ and then cultured for 24 hours in the presence of conditioned media from either MSI or MSS tumors. Unsupervised clustering of the resulting membrane-protein intensities revealed a striking separation between the two treatment groups (Figure 3E), demonstrating that tumor-secreted factors profoundly reprogram surface-protein distribution (all detected proteins and statistically significant differences are reported in Supplementary Tables S1-S6).

Pathway analysis of differentially abundant proteins revealed that exposure to MSS-conditioned media leads to substantial molecular reprogramming (Figure 3F; Supplementary Figure 11A). Affected pathways were primarily associated with immune regulation, metabolic activity, and post-translational modifications, suggesting that the MSS-associated secretome exerts a broad modulatory effect on mediators of immune cell function and intercellular communication. Among the altered pathways, we specifically investigated those that could reflect tumor-intrinsic mechanisms actively contributing to immune evasion within a short timeframe (5–24 hours assay). Given the evolutionary conservation and the well-established role of glycosylation in shaping immune escape, remodeling the tumor microenvironment, and modulating T cell–mediated recognition and immunotherapy response (26,27,28,29,30,31), we focused on this process. We therefore analyzed the subset of genes that were both significantly altered and annotated within the enriched pathways, with particular attention to those functionally linked to glycosylation. This analysis is summarized in the alluvial plot (Figure 3G), which illustrates the connection between enriched pathways and glycosylation-related genes, their respective gene functions, and broader functional macro-categories. Strikingly, a substantial proportion of the altered genes exhibited direct or indirect associations with glycosylation, underscoring the prominent role of this modification in mediating the proteomic effects of MSS-derived secreted factors. The intersection between significantly regulated membrane proteins and glycosylation-related pathways across individual PDOs is shown in Supplementary Figure 11B.

To functionally validate the impact of glycosylation on immune recognition, we repeated the MSI T cell recognition assay in the presence of conditioned media from both MSI and MSS sources (Figure

2B–D). In this setting, we co-treated organoids with the O-glycosylation inhibitor benzyl-α-GalNAc and the glycosyltransferase inhibitor lithocholic-O-aspartate (Supplementary Figure 12). Remarkably, inhibition of glycan elongation fully restored T cell recognition in all MSI samples, reaching levels comparable to untreated controls (Supplementary Figure 12). These results demonstrate that tumor-derived soluble factors can induce glycosylation-dependent changes that directly interfere with T cell–tumor interface, potentially promoting immune escape.

To further determine whether glycosylation directly modulates tumor cell susceptibility to T cell recognition, we performed additional co-culture experiments in the absence of conditioned media using antigen-loaded PDOs. Consistent with our previous observations, MSS organoids induced significantly lower T cell activation compared with MSI organoids. Importantly, pharmacological inhibition of glycosylation had minimal impact on MSI samples but restored T cell activation in MSS organoids to levels comparable to MSI controls (Figure 3H), confirming a direct role of glycosylation in limiting T cell responsiveness in MSS tumors.

Cumulatively, these findings indicate that MSS CRCs are capable of actively disrupting T cell recognition and activation, revealing a novel tumor cell-intrinsic mechanism of immune escape. Our data identify the tumor secretome as a key regulator of immune recognition dynamics, specifically impairing T cell engagement and the formation of a stable tumor–immune synapse. Surface proteomic profiling further demonstrated that tumor-derived factors extensively remodel the tumor membrane landscape, with glycosylation emerging as a central, functionally relevant modification. Together, these results highlight a previously underappreciated pathway of immune evasion mediated by secretome-driven modulation of the tumor cell surface.

Discussion

Patients diagnosed with microsatellite-instable (MSI) colorectal cancer (CRC) often benefit from therapies based on immune checkpoint blockade, while those with microsatellite-stable (MSS) tumors generally do not (5,10,11,13). The prevalent view is that MSI tumors are recognized by the immune system owing to their elevated mutational/neoantigen repertoire. However, emerging evidence suggests that factors beyond neoantigen count play a pivotal role in modulating the therapeutic response. In the current study we aimed to dissect the biological mechanisms responsible for the different immune response in MSS compared to MSI tumors.

To this end we first developed an experimental platform wherein both MSS and MSI tumors presented the same antigen (Mart-1_{ELA}) at an identical concentration via the same presenting molecule (HLA-A2) to a homogeneous T cell population engineered to express 1D3-TCR. This design

ensures that the main variables in the tumor-host interaction are the intrinsic features of the cancer cells. MSS tumors consistently displayed a reduced recognition by the immune system. Impaired immune activation was accompanied by a common biological profile as defined by distinct effector molecules and activation markers such as IFNγ, TNFα, Granzyme-A, Granzyme-B and CD137. Functional assessment of T cell cytotoxic capacity in the presence of MSS and MSI cells revealed that while MSI tumors were efficiently killed by the engineered T cells, MSS tumors remained unaffected.

The experimental platform we implemented in this study can be broadly used for understanding how distinct cancer subtypes modulate T cell reactivity. Moreover, these results show that MSS tumors are intrinsically recalcitrant to T cell-mediated recognition and killing. How tumor intrinsic factors modulate tumor-host interaction, immune recognition and the ensuing killing have remained largely unrecognized. Our findings have a strong clinical relevance: even if the TMB of MSS tumors were successfully augmented by experimental strategies, for example with mutagenic/alkylating agents, the native resistance mechanisms of MSS tumors could still hamper an effective immune-mediated control, as shown in our current work. The same would apply if a strongly immunogenic neoantigen is successfully introduced in MSS CRC. In this regard genetic or pharmacological approaches designed to disable the MMR pathway rather than simply increasing the TMB could be advantageous as we and others have shown (16,17,18,32,33,34).

After establishing that tumor intrinsic factors are instrumental for resistance and response to immune surveillance, we set out to characterize the biological basis for this phenotype.

We focused on the tumor secretome as a potential contributor to the observed differences. Proteomic profiling revealed distinct differences in the soluble factors released by MSI and MSS tumors during antigen-specific T cell engagement. Notably, MSS tumors shaped a secretory milieu that appeared less supportive of immune activation, characterized by reduced lymphocyte recruitment and weakened pro-apoptotic signaling, suggesting a shift toward an immune-suppressive environment. To functionally test whether tumor-derived soluble factors directly impact T cell activity, we performed secretome functional experiments. The results were striking: conditioned media derived from MSS tumor organoids significantly reduced T cell recognition of MSI tumor cells. Furthermore, exposure of engineered T cells to MSS-conditioned media was sufficient to impair their cytotoxic ability against MSI targets. These findings support the notion that MSS tumors engage tumor-intrinsic secretory programs capable of interfering with effective immune recognition.

Importantly, the effects mediated by MSS-conditioned media were not due to a generalized impairment of T cell function. T cells retained their viability, proliferative capacity, and remained fully responsive when stimulated by professional antigen-presenting cells, even in the presence of tumor-derived soluble factors. This indicates that the observed phenotype is not the result of broad

immunosuppression, but rather reflects a mechanism that specifically interferes with the physical interaction between T cells and tumor cells.

By analyzing the dynamics of T cell–tumor engagement, we observed a reduced frequency and strength of T cell contact in the presence of MSS tumors or MSS-derived conditioned media, suggesting that the impaired recognition involves active modulation of the tumor–immune interface.

To further confirm our findings, we used an unbiased surface proteomic approach, which uncovered a widespread remodeling of the tumor membrane in response to MSS-derived factors. Among the pathways altered by MSS-conditioned media, we primarily observed changes in metabolism, immune-related molecules, antigen presentation, and cell–cell communication. Glycosylation, while not explicitly highlighted as a top enriched pathway in our analysis, emerged from the profile of proteins involved as a likely modification impacting key molecules at the immune synapse. Our data, together with previous reports emphasizing the importance of metabolic rewiring, especially glycosylation, in immune escape, support the hypothesis that this post-translational modification reshapes the tumor cell surface (30,31,35,36). Indeed, glycosylation is an evolutionarily conserved mechanism through which tumor cells remodel their surface to evade immune detection, with aberrant glycan patterns shown to alter receptor-ligand interactions, modulate antigen presentation, and disrupt immune synapse formation across multiple cancer types (26,27,28,29,30,31). Our findings build on this established framework and uncover a previously unrecognized layer of complexity: in MSS CRC, tumor-secreted factors are sufficient to induce glycosylation-dependent surface remodeling on neighboring tumor cells, extending immune evasion beyond cell-autonomous mechanisms.

Given the known role of glycosylation in immune modulation, we tested its functional relevance in our system. Strikingly, pharmacological inhibition of glycosylation fully rescued T cell recognition of MSI tumors treated with MSS-conditioned media, restoring recognition to control levels. Critically, glycosylation blockade also significantly enhanced T cell activation against native MSS PDOs, restoring it to levels comparable to those observed with MSI targets, implicating glycosylation-dependent immune evasion as an intrinsic feature of MSS tumor cells themselves. These results suggest that tumor-secreted factors can modulate the tumor cell surface in trans through glycan remodeling, impairing the formation of a productive immune synapse and ultimately weakening immune recognition. Importantly, this effect operates primarily at the tumor cell surface rather than through direct modulation of T cell function. Siglec receptors, lectin-type receptors known to dampen immune responses upon recognition of sialylated glycans (29), were virtually absent on TCR-transduced T cells and were not induced by glycosylation inhibitor exposure. Consistently, pharmacological glycosylation blockade at the concentrations used in co-culture assays left T cell viability, proliferation, and

activation capacity fully intact. The glycosylation-dependent immune evasion we describe is therefore a tumor-intrinsic phenomenon, acting at the interface between cancer cells and T cells. While pharmacological inhibition proved effective, we also explored enzymatic deglycosylation using PNGase F as a complementary approach. Although PNGase F efficiently removed glycans from denatured protein extracts, it failed to act on intact viable PDOs. This is consistent with the known biochemical requirements of glycan-remodeling enzymes, which depend on protein denaturation to access glycosylation sites, rendering them inherently incompatible with live cell systems where proteins retain their native conformation. This underscores the value of pharmacological inhibitors as the most suitable strategy to interrogate glycosylation-dependent mechanisms in intact live model systems.

The identity of the upstream secreted mediator(s) responsible for triggering glycan remodeling remains an open and important question. Targeted secretome profiling of MSS PDOs using a 96-plex immuno-oncology panel did not converge on a single dominant factor, pointing instead toward a combinatorial or non-canonical signal, potentially involving extracellular vesicles, metabolites, or lipid mediators, that falls outside the scope of antibody-based panels. In line with this, analysis of publicly available colorectal cancer RNA-seq datasets revealed no coordinated transcriptional upregulation of glycosylation pathways in MSS versus MSI tumors, suggesting that the observed surface remodeling reflects post-transcriptional or post-translational regulation rather than a hardwired transcriptional program. Dissecting these upstream mechanisms will be a key priority for future work.

It is therefore conceivable that, beyond lacking the high neoantigen load characteristic of MMR-deficient tumors, MSS tumors may actively shape an immunosuppressive secretome that impairs immune recognition. Our findings highlight the tumor secretome as a critical modulator of immune responsiveness and suggest that targeting secreted factors from MSS tumors may provide new opportunities to overcome resistance in MSS cancers. In addition to informing new therapeutic strategies, this work provides a rationale for integrating secretome profiling into clinical decision-making. By identifying secretome-driven mechanisms that influence immune recognition, we shed light on new strategies for patients' stratification, enabling the design of combination treatments tailored to the tumor's immunomodulatory profile. Such an approach could help extend the benefits of immunotherapy to patients with MSS tumors, who currently show limited responses to immune checkpoint inhibitors.

Importantly, while our study implicates glycosylation-dependent changes as key contributors to immune evasion, these mechanisms are unlikely to be exclusive. Other intrinsic pathways may similarly mediate resistance to T cell pressure in MSS tumors, despite the presence of targetable antigens. This highlights a central insight of our work: MSS tumors possess an active, biologically

encoded resistance to immune attack, beyond antigenicity alone. Crucially, our experimental strategy provides a framework to uncover such intrinsic immune escape mechanisms, offering a broadly applicable approach to dissecting tumor immunoresistance across cancer types, and not limited to the MSS/MSI CRC context.

In conclusion, our data provide new transforming knowledge on how tumor cells interact and modulate the immune system of the host. Combinatorial treatments, designed to elevate neoantigen loads while at the same time neutralizing tumors' intrinsic resistance should be explored to foster immune surveillance of CRC tumors which are currently not eligible for immunotherapeutic treatment.

Material and Methods

Human subjects

Tumor tissue was collected from patients aged 18 years or older with stage I, II, III or IV resectable colorectal cancer, treated at Grande Ospedale Metropolitano Niguarda, Instituto Nazionale dei Tumori, Istituto Europeo di Oncologia in Milan, AUSL della Romagna in Ravenna, and Ospedale di Santa Maria della Misericordia in Perugia. All patients provided written informed consent in accordance with the Declaration of Helsinki. The study was conducted under the ALFAOMEGA Master Observational Trial (NCT04120935), sponsored by IFOM ETS- The AIRC Institute of Molecular Oncology and approved by the Ethical Committee of each participating center. Tumor tissue for MSI_05 and MSI_06 was collected at the Netherlands Cancer Institute. The study (NL48824.031.14) was approved by the Medical Ethical Committee of the Netherlands Cancer Institute – Antoni van Leeuwenhoek hospital and written informed consent was obtained from both patients.

Organoid culture

Tumor tissue was obtained by surgical resection and processed within 24 hours CRC organoids were established essentially as described in Cattaneo C.M. et al., 2020 and Dijkstra K.K. et al., 2018 (22,23). Briefly, tumor tissue was cute into small pieces and further processed using Tumor Dissociation kit (Miltenyi Biotec, cat. no 130-095-929), before embedding in Cultrex Reduced Growth Factor Basal Membrane Extract type 2 (RGF-BME-2, R&Dsystem, cat. no 3533-005-02). CRC organoid medium is composed of Ad-DF (Advanced DMEM/F12; Gibco, cat no 12634010), supplemented with 2 mM GlutaMAX Supplement (Gibco, cat. no 35050061), 10 mM HEPES (Euroclone, cat. no ECM0180L) and 100/100 u/mL Pencillin/Streptomycin (Euroclone, cat. no ECB3001L), 10% Noggin-conditioned medium, 20% R-spondin1-conditioned medium, 1x B27 supplement without vitamin A (Gibco, cat. no

12587010), 1.25 nM N-Acetylcysteine (Sigma-Aldrich, cat. no A9165), 10 mM Nicotinamide (Sigma-Aldrich, cat. no N0636), 50 ng/mL human recombinant EGF (PeproTech, cat. no AF-100-15), 500 nM A83-01 (Tocris, cat. no 2939), 3 µM SB202190 (Sigma-Aldrich, cat. no S7067) and 10 nM prostaglandin E2 (Cayman Chemicals, cat. no 14010-1). Organoids were passaged approximately every 1-2 weeks by incubating in TrypLE Express (Gibco, cat. no 12605028) for 5-10 min at 37°C to dissociate organoids to single cells and replating in fresh BME. After passaging, 10 µM Y-27632 (Selleckchem, cat. no S1049) was added to CRC medium for the first 2-3 days. Organoids were cryopreserved in 10%DMSO/FBS (Euroclone, cat. no. EMR385250; Sigma-Aldrich, cat. no. F7524). Organoids were regularly checked for mycoplasma contamination. The identity of each cell line was checked before starting each experiment and after every genomic DNA extraction by GenePrint 10 system (Promega, cat. no. B9510), through short tandem repeats at 16 different loci.

Immunohistochemistry

Organoids were recovered from BME, pelleted and fixed in 4% paraformaldehyde for 2 hours at room temperature. Samples were embedded in paraffin blocks using Diapath automatic processator. Sections of approximately 4 µm were cut and counterstained with Hematoxylin and Eosin (Diapath) according to standard protocol. Samples were mounted in Eukitt (bio-Optica) for histopathological analysis. For assessment of mismatch repair status, immunohistochemistry was performed according to standard protocols. Paraffin was removed with xylene and the sections were rehydrated in graded alcohol. Antigen retrieval was carried out using preheated target retrieval solution for 30 min or using 10mM citrate buffer (anti-MSH2) or Tris-EDTA buffer pH 9.0 (anti-MLH1, anti-MSH6 and anti-PMS2) heated for 30 minutes and blocked and endogenous peroxidase was quenched with 3% hydrogen peroxide in distilled water for 10 minutes at RT. Tissue sections were blocked with FBS serum in PBS for 60 min and incubated 2h with the following primary antibodies, diluted 1:30: MLH1, clone G168-15 (BIOCARE MEDICAL, cat. no PM 220 AA, RRID:AB_10581025); MSH2, clone FE11 (BIOCARE MEDICAL, cat. no PM 219 AA, RRID:AB_10581790); MSH6, clone 44 (BIOCARE MEDICAL, cat. no. PM265 AA, RRID:AB_10581791); PMS2, clone A16-4 (BIOCARE MEDICAL, cat. no. PM344 AA, RRID:AB_10581487). The antibody binding was detected using a polymer detection kit (GAM-HRP, Microtech) followed by a diaminobenzidine chromogen reaction (Peroxidase substrate kit, DAB, SK-4100; Vector lab). All sections were counterstained with Mayer's hematoxylin and visualized using a bright-field microscope (Leica DM750). Samples were analyzed for the absence or presence of nuclear staining of the MMR proteins. The IHC results were confirmed by a pathologist who was blinded to the results.

Organoid surface staining

Organoids were dissociated to single cells using TrypLE Express, with or without 24 hours pre-incubation with 200 ng/mL IFNγ (PeproTech, cat. no 300-02). Tumor cells were washed in FACS buffer (PBS supplemented with 5 mM EDTA and 1% BSA) and stained using the following antibodies: mouse anti-human HLA-A,B,C-PE (BD, cat. no 555553, RRID:AB_395936; clone G46-2.6, used 1:50), mouse anti-human HLA-A2-APC (BD, cat. no 561341, RRID:AB_10646036; clone BB7.2, used 1:50), mouse anti-human HLA-DP/DQ/DR-FITC (BD, cat. no 550853, RRID:AB_393926; clone Tü39, used 1:50), mouse anti-human CD274-APC (eBioscience, cat. no 17-5983-41, RRID:AB_10597280; clone MIH1, used 1:200). Antibodies were used according to manufacturer's instruction. To exclude dead cells, we used labelling with near-IR viability dye (Invitrogen, cat. no L10119), Zombie Aqua Fixable viability kit (Biolegend, cat. no. 423101), or DAPI, following manufacturer's instruction. Cells were recorded with a Canto II flow cytometer or Cytoflex S flow cytometer.

T cell engineering and culture

Healthy donor-derived T cells are engineered as described in Cattaneo C.M. et al., 2023 (21). Briefly, TCR α and β variable sequences of the selected TCR were synthesized and subcloned into a modified pMP71 retroviral vector, that contains mouse TCR constant regions and the puromycin N-acetyltransferase resistance gene. Retrovirus was produced by transfecting FLY-RD18 packaging cells (RRID:CVCL_8871) with pMP71-TCR plasmid DNA using Xtremegene 9 transfection reagent (Merck, cat. no 6365779001). In the meantime, $CD8^+$ T cells were isolated from healthy donor PBMCs using the $CD8^+$ T Cell Isolation Kit (Miltenyi Biotec, cat. no 130-096-495) and stimulated with 5 µg/mL plate bound aCD3/CD28 (eBioscience, cat. no 16-0037-85, clone OKT-3, RRID:AB_468855; eBioscience, cat. no 16-0289-81, clone CD28.2, RRID:AB_468926) in T cell medium (composed of RPMI 1640 medium (Euroclone, cat. no ECB9006L), supplemented with 10% human AB serum (Euroclone, cat. no ECS0219D), 100/100 u/mL Pencillin/Streptomycin, 2 mM Ultraglutamine I and with 150 U/mL human recombinant IL-2 (R&Dsystem, cat. no 200-IL). After 48 h, retroviral supernatants were collected and used to infect prestimulated CD8+ T cells by spinoculation (2,000 g for 90 min) in Retronectin (Takara, cat. no T100B)-coated plates. Transduction efficiency was measured 72 h later by staining with anti-mouse TCRβ - PE (BD, cat. no 561081; clone H57-597, RRID:AB_10563767, used 1:150) and analysed by flow cytometry. TCR-transduced T cells were then selected with 2.5 µg/mL puromycin (Vinci-Adipogen, cat. no AG-CN2-0078-M100). Then, transduced T cells were expanded using the rapid expansion protocol REP with a 1:1 mixture of RPMI 1640 and AIM-V medium (Gibco, cat. no 12055091) supplemented with 5% human AB serum, 30 ng/ml anti-CD3 antibody and 3,000 U/ml human recombinant IL-2, in the presence of irradiated (40 Gy) allogeneic PBMCs (200:1 feeder/T

cell ratio). After 7 days of REP culture, medium was refreshed with new IL-2 every 2 days, for a total REP culture time of 14 days. After REP, transduced T cells were cryopreserved in 10%DMSO/FBS or kept in culture at ~$2e^6$ cells/mL in T cell medium.

Tumor recognition assays

Tumor organoids were previously stimulated with 200 ng/mL IFNγ (Peprotech, cat. no 300-02) for 24 hours. After dissociation into single cells using TrypLE express (Gibco, cat. no 12605028), organoids were resuspended in PBS containing varying concentrations of MART-1 peptide (ELAGIGILTV or EAAGIGILTV; 0/0.02/0.1/0.5 µM) and incubated for 30 minutes at 37°C. Organoids were then washed twice with PBS and resuspended in T cell medium. For glycosylation blocking experiments, tumor organoids were pre-treated post-dissociation with 2.5 µM Benzyl-α-GalNAc (MedChemExpress, cat. no. HY-129389) and 100 µM Lithocholic acid O-aspartate (Lith-O-Asp; MedChemExpress, cat. no HY-112415) for 2 hours at 37°C. Following washes, these organoids were pulsed with 0.02 µM MART-1_{ELA} peptide for 30 minutes at 37°C before final washing and resuspension in T cell medium.
TCR-transduced CD8+ T cells were seeded with tumor organoids at a 1:2 T cell-to-organoid ratio in anti-CD28 (eBioscience, cat. no 16-0289-81, clone CD28.2, RRID:AB_468926) coated U-bottom 96-well plates, cultured in either standard T cell medium or conditioned media as specified. For glycosylation inhibition assays, media were supplemented with 0.25 µM Benzyl-α-GalNAc and 10 µM Lith-O-Asp throughout co-culture. When applicable, 20 µg/mL anti-PD1 blocking antibody (nivolumab) was added. T cells cultured without target cells served as negative controls, while stimulation with 50 ng/mL phorbol 12-myristate 13-acetate (Sigma-Aldrich, cat. no 19-144) and 1 µg/mL ionomycin (Sigma-Aldrich, cat. no I9657) functioned as positive controls.
For CD137 surface expression, after 24 hours incubation with tumor organoids, T cells were washed twice in FACS buffer and stained with anti-human CD3–PerCP-Cy5.5 (BD, cat.no 332771, RRID: AB_2868620, clone SK7, 1:20), anti-human CD8-BV421 (BD, cat. no 562429, RRID: AB_11153676, clone RPA-T8, 1:200), anti-mouse TCRβ–PE (BD, cat. no 561081, RRID: AB_10563767, clone H57-597, 1:150), anti-human CD137–APC (BD, cat. no 550890, RRID: AB_398477, clone 4B4-1, 1:30), and near-IR viability dye (Invitrogen, cat. no L10119) for 30 minutes at 4°C in the dark. Cells were washed and acquired on a Canto II flow cytometer. For intracellular IFNγ analysis, after 1 hour co-culture with tumor organoids, Golgi-Plug (BD, cat. no 555029) and Golgi-Stop (BD, cat. no 554724) were added, and incubation continued for 4 hours. Cells were washed twice, stained with anti-human CD3–PerCP-Cy5.5, anti-human CD8-BV421, anti-mouse TCRβ–PE, and viability dye, fixed, permeabilized, and stained intracellularly for IFNγ (BD, cat no. 554702, RRID: AB_398580, clone B27, 1:50) using the

Cytofix/Cytoperm kit (BD, cat. no 554714, RRID: AB_2869008). Cells were then resuspended in FACS buffer and recorded with a Canto II flow cytometer.

Tumor killing assay

Patient derived tumor organoids were previously stimulated with 200 ng/mL IFNγ (Peprotech, cat. no 300-02) for 24hr. Then, after dissociation into single cells using TrypLE express (Gibco, cat. no 12605028), organoids were stained with 100 nM CellTrace FarRed (Invitrogen, cat. no C34564) in PBS for 20 minutes at 37°C, and subsequently washed twice with 10%FBS/PBS. Next, tumor organoids were resuspended in PBS in the presence of 0 or 0.02 μM of MART-1 peptide (ELAGIGILTV). After 30 minutes incubation at 37°C, organoids were washed twice in PBS and resuspended in T cell medium. Tumor organoids were then seeded alone or with the TCR-transduced CD8+ T cells (5:1 T cell / organoid ratio) in anti-CD28 (eBioscience, cat. no 16-0289-81, clone CD28.2, RRID:AB_468926) coated U-bottom 96-well plates, in T cell medium or conditioned media (collected as described below) supplemented with 20 μg/mL anti-PD1 blocking antibody. After 24 hr incubation, pictures of each well were taken with a fluorescence microscope, for the quantification of the FarRed signal, using FIJI. Additionally, a flow cytometry-based quantification was performed. Organoids and T cells were collected and dissociated into single cells with TrypLE Express. 7.46 μm AccuCount blank counting beads (Spherotech, cat. no ACBP-70-10) were added to each well in equal number. Cells were then washed twice in FACS buffer and stained with DAPI and recorded with a Canto II flow cytometer.

Cytokines, chemokines and immunomodulatory molecules release assay

For the analysis of cytokine, the supernatants of the CD137-mediated recognition assay were collected after 24 hours in culture. Supernatants were immediately frozen and preserved at −80˚C. Supernatants were thawed on ice and the presence of the indicated cytokines was detected using the Cytometric Beads Array Human IFN-γ Flex Set (BD, cat. no 558269, RRID: AB_2869127) or the LEGENDplex Human CD8/NK panels (BioLegend, cat. no 741065), according to the manufacturers' instructions. For the analysis of chemokines, the conditioned media of the different organoids was collect as described below and used as supernatant. Supernatants were used fresh or immediately frozen, preserved at −80˚C and thawed on ice when needed. The presence of the indicated chemokines was detected using the LEGENDplex Human Proinflammatory Chemokine Panel 1 (BioLegend cat. no 741081) and Olink ® Immuno-Oncology Target 96 kit, according to the manufacturers' instructions.

Conditioned media collection

Tumor organoids were previously stimulated with 200 ng/mL IFNγ (Peprotech, cat. no 300-02) for 24 hours. Then, after dissociation into single cells using TrypLE express, organoids were seeded in fresh T cell medium at $2.5e^5$ cells/mL. 24 hours later, supernatant was collected and spin at 1500 rpm for 5 minutes to remove any debris. Supernatant was used fresh or immediately frozen and preserved at -80˚C.

T cells viability, functionality and proliferation assay

To determine cell viability, TCR-transduced $CD8^+$ T cells were seeded at the concentration of $1x10^6$ cells/ml in anti-CD28 (eBioscience, cat. no 16-0289-81, clone CD28.2, RRID:AB_468926) coated U-bottom 96-well plates, in T cell medium or conditioned media (collected as described). CellTiter-Glo™ Luminescent Cell Viability Assay (Promega, cat. no G7573) was used at the time of seeding and again after 24h. Luminescence was measured at Envision (Perkin Elmer).

Activation of T cells was evaluated by intracellular IFNγ expression. Briefly, HLA-$A2^+$ immortalized B cells (20) were incubated with 0 or 0.02 μM of Mart-1_{ELA} peptide for 30 minutes at 37°C, followed by two washed in PBS. Subsequently, B cells were resuspended in T cell medium or conditioned media. TCR-transduced $CD8^+$ T cells were then seeded with B cells (1:2 T cell / Bcell ratio) in anti-CD28 coated U-bottom 96-well plates, using T cell medium or conditioned media (collected as described). Golgi-Plug (BD, cat. no 555029) and Golgi-Stop (BD, cat. no 554724) was added to the coculture and incubated for an additional 4 hours. Following co-culture, cells were washed twice in FACS buffer and stained with anti-human CD3-PerCP-Cy5.5 (BD, cat.no 332771, RRID: AB_2868620, clone SK7, 1:20), anti-human CD8-BV421 (BD, cat. no 562429, RRID: AB_11153676, clone RPA-T8, 1:200), anti-mouse TCRβ-PE (BD, cat. no 561081, RRID: AB_10563767, clone H57-597, 1:150) and near-IR viability dye (Invitrogen, cat. no L10119) for 30 min at 4˚C. Cells were washed twice in FACS buffer, fixed, and stained for intracellular IFNγ (anti-human IFNγ-APC, (BD, cat. no 554702, RRID: AB_398580, clone B27, used 1:50) using the Cytofix/Cytoperm kit (BD, cat. no 554714, RRID: AB_2869008), according to manufacturer's instructions. Cells were then resuspended in FACS buffer and recorded with a Canto II flow cytometer.

To determine T cell proliferation, TCR-transduced T cells were labelled with 100 nM CellTrace FarRed (Invitrogen, cat. no C34564) following manufacturer's instruction. Then, T cells were seeded at the concentration of $1x10^6$ cells/ml in anti-CD28 coated U-bottom 96-well plates, with or of Mart-1_{ELA} -loaded B cells (2:1 T cells/B cell ratio), for stimulated and unstimulated conditions, respectively. The assay was performed in T cell media or in MMRp-derived conditioned media. After 72 hours, cells were resuspended in FACS buffer, stained with DAPI and recorded with Cytoflex S flow cytometer.

T cell engagement assay

To quantify physical engagement between T cells and tumor cells, we employed a high-content imaging assay based on co-cultures of fluorescently labeled T cells and tumor organoids. Two days prior to the assay, patient-derived tumor organoids were enzymatically dissociated into single cells and passed through a 40 µm cell strainer to ensure uniform organoid size. Organoids were re-aggregated and maintained in culture for 24 hours, then stimulated with 200 ng/mL IFNγ for an additional 24 hours to enhance antigen presentation. On the day of the assay, organoids were labeled with Cytolight Red (Sartorius, cat. no 4705) according to the manufacturer's instructions and pulsed with 0.02 µM MART-1_{ELA} peptide for 30 minutes at 37°C. Organoids were seeded in flat-bottom 96-well plates at 1,000 organoids per well, corresponding to approximately 10,000 single-cell equivalents. T cells were labeled with CellTrace CFSE Cell Proliferation Kit (Invitrogen, cat. no C34554) following the manufacturer's protocol and added to the wells at an effector-to-target (E:T) ratio of 1:2. Co-cultures were maintained in either standard T cell medium or tumor-conditioned medium (collected as described above), supplemented with 20 µg/mL anti–PD-L1 blocking antibody (nivolumab). Plates were imaged after 48 hours using the Incucyte live-cell analysis system. T cell engagement was quantified using FIJI, by measuring the proportion of T cells in direct contact with tumor organoids. Engaged T cells were expressed as a percentage of total segmented T cells per field of view.

T cell avidity assay

The binding strength between T cells and tumor cells was assessed using the z-Movi® Cell Avidity Analyzer (LUMICKS), according to the manufacturer's protocol with custom adaptations. Tumor organoids were first stimulated with 200 ng/mL IFNγ for 24 hours, then enzymatically dissociated into single cells. Tumor cells were seeded onto z-Movi glass-bottom flow chambers at a density of 1.5×10^8 cells/mL to form a confluent monolayer. Depending on the experiment, the glass surface was pre-coated with either poly-L-lysine (Sigma-Aldrich, cat. No P4707) or concanavalin A (Sigma-Aldrich, cat. no C2010). Peptide loading was performed directly on the adhered tumor cells using 100 µM MART-1_{ELA} peptide for 1 hour at 37°C. For experiments involving conditioned media, tumor cells were pre-incubated with the indicated CM for 24 hours prior to the assay, and the same CM was used during the measurement.

Effector T cells were labeled with CellTrace Far Red (Invitrogen, cat. no C34564) and resuspended at 1×10^7 cells/mL. During the assay, individual T cells in suspension were acoustically positioned onto the

tumor monolayer. The contact time between T cells and tumor cells was set to 10 minutes (docking phase), after which a gradually increasing acoustic force was applied to detach the T cells.
The output was represented as the percentage of bound T cells as a function of the applied force, generating binding strength curves for each condition. Data were acquired and processed using the LUMICKS software suite.

Membrane proteome after exposure to conditioned media

MSI-tumor organoids were previously stimulated with 200 ng/mL IFNγ for 24 hours, as performed in the functional assays. Then, organoids were dissociated into single cells using TrypLE express and resuspended in conditioned media (collected as previously described). Cells were seeded in a 24-well plate and incubated for 24 hours at 37°C. After incubation, tumor cells were collected, washed in PBS and processed for membrane protein extraction using the Mem-PER™ Plus Membrane Protein Extraction Kit (Thermo Scientific, cat. no. 89842), following the manufacturer's instructions. Membrane proteome was quantified using the Pierce™ BCA Protein Assay Kits (Thermo Scientific, cat. no. 23225). Then, the membrane protein fraction was digested for LC-MS/MS analysis. Briefly, 25 µg of membrane fraction were resuspended in 200 µl of UA buffer (100 mM Tris HCl pH 8.0, 8 M urea) and transferred into microcon filters with 10 kDa cutoff (Millipore). After four washes with 300 µl UA buffer, cysteine reduction and alkylation were performed adding 10 mM TCEP (Thermo scientific) and 40 mM 2-Chloroacetamide (Sigma-Aldrich) in UA buffer for 30 min at room temperature. After two washes with UA buffer and one with 100 mM Tris HCl, pH 8.0, protein in-solution digestion was performed by incubating each sample in 100 µl of 100 mM Tris HCl, pH 8.0, supplemented with 1 µg of trypsin overnight at 37°C. Then, an additional incubation with 1 µg of trypsin for 3 h was performed. The obtained peptides were collected by centrifugation and purified on a C18 StageTip.

Global and membrane proteomics MS analysis

1.5 µl of digested sample was injected onto an Exploris 480 mass spectrometer (Thermo Scientific) equipped with FAIMS device (Thermo Scientific). Columns were packed in-house with ReproSil-Pur C18-AQ beads (Dr. Maisch Gmbh, Ammerbuch, Germany), 1.9 µm of diameter, using a high-pressure bomb loader (Proxeon, Odense, Denmark).
Peptides separation was achieved with a linear gradient from 95% solvent A (2 % ACN, 0.1% formic acid) to 41% solvent B (80% ACN, 0.1% formic acid) over 124 min and from 41% to 100% solvent B in 9 min at a constant flow rate of 0.25 µL/min, with a single run time of 131 min. The mass spectrometer was operated in data-independent acquisition (DIA) mode with the following parameters: charge state: 2–6, MS1 resolution = 120,000, precursor range 400–1000 m/z, MS1 automatic gain control

target=3×106 (300%), MS1 maximum injection time=55ms, MS2 resolution=30,000, MS2 automatic gain control target=10×106 (1000%), MS2 maximum fill time=Auto, Radio Frequency lens 40%, and MS2 HCD collision energy %=32, 30 m/z isolation window. The MS2 scan range was Auto, and the loop control was set to All.

The FAIMS device was operated with voltages −50V and −70V, with a total carrier gas flow of 3.7L/min at 300°C for Ion transfer tube temperature.

DIA MS Analysis and Database Search

The DIA raw files of FAIMS-DIA were searched by Spectronaut (SN) vs 18. These searches were done in direct DIA mode. The default BGS factory settings, using UniProt cp Human proteome reference, were used. For DIA searches comparison, Trypsin was selected as the digestion enzyme. Carbamidomethylation was selected as a fixed modification, while methionine oxidation and N-terminal acetylation were selected as variable modifications. FDRs of PSMs and peptide/protein groups were set to 0.01. “Area” MS2 quantity type was used with Cross-Run Normalization “ON”. Data are available via ProteomeXchange (37) with identifier PXD066343.

Data Availability Statement

All data generated and/or analyzed during this study are included in this published article. Additional information can be requested to the corresponding authors. The proteomics data have been deposited in the ProteomeXchange Consortium via the PRIDE partner repository with the dataset identifier PXD066343.

Acknowledgments

The authors thank Sara Volorio and Domenico Sardella, from the DNA Sanger Sequencing Facility at Cogentech. The authors also thank the IFOM ETS Cogentech Proteomics and Metabolomics Core Facility (RRID:SCR_026937), where the proteomics data were generated. The authors thank Chiara Camisaschi and Ilaria Montali at the Flow Cytometry Core of IRCCS Humanitas Research Hospital for their support. The authors thank Fondazione Oncologia Niguarda for supporting the logistics of samples procurement. The authors thank the tissue culture facility at IFOM ETS for their support. The authors thank the ALEMBIC facility and the FRACTAL facility at IRCCS Ospedale San Raffaele for their support. The research leading to these results has received funding from: European Research Council (ERC) under the European Union’s Horizon 2020 research and innovation programme (TARGET, grant agreement n. 101020342) (A.B.); AIRC under 5 per Mille 2018 – ID. 21091 program – P.I. Bardelli

Alberto (A.B.); AIRC under IG 2018 – ID. 28922 project – P.I. Bardelli Alberto (A.B.); IMI contract n. 101007937 PERSIST-SEQ (A.B.); HORIZON ERC Proof of Concept Grants (CHIMERA, grant agreement n. 101292472) (A.B.). Views and opinions expressed are however those of the author(s) only and do not necessarily reflect those of the European Union or the European Research Council. Neither the European Union nor the granting authority can be held responsible for them. W.S. is supported by the Dutch Cancer Society Young Investigator Grant (grant No. 2020-1/12977) and ZonMw Translational Research Program 2 (grant No. 446002001). C.M.C. was supported by Fondazione Umberto Veronesi and by Fondazione AIRC per la ricerca sul cancro ETS (AIRC Fellowship for Italy, grant number 26789). S.S. and G.M. are PhD students within the European School of Molecular Medicine (SEMM). G.M. received honoraria from COR2ED. CB is supported by AIRC (Ig 24965) and AIRC under 5 per Mille 2019 – ID. 22737 program – P.I. Chiara Bonini (C.B.), Italian Ministry of Research and University (PRIN 2022SLL3YZ), Italian Ministry of Health (Research project on CAR-T cells for hematological malignancies and solid tumors; RF-2019-12370243, RF-2021-12373598); EU (T2Evolve, Join4ATMP). An.B. is supported by AIRC IG 27098 grant. Figure 1A and Figure 2B were created with BioRender.com. AI-assisted technologies were used solely for language editing purposes.

Author contribution

Conceptualization: C.M.C, A.B.; Data curation: C.M.C, S.S.; Resources: G.M., W.S., L.L., S.Si., S.M., E.E.V., An.B., C.B., A.B.; Formal analysis: C.M.C, S.S., V.M., V.O., C.C.; Methodology: C.M.C., S.S.,V.M., V.O., R.C., C.C., Z.M.; Visualization: C.M.C, S.S.; Supervision: C.M.C., G.G., A.B.; Funding acquisition: A.B.; writing – original draft: C.M.C., S.S.; writing – review and editing: C.M.C., S.S., G.M., W.S., L.L., C.B., S.Si., E.E.V., G.G., A.B.

References

1. Network CGA. Comprehensive molecular characterization of human colon and rectal cancer. Nature 2012;487:330-7
2. Koopman M, Kortman GA, Mekenkamp L, Ligtenberg MJ, Hoogerbrugge N, Antonini NF, et al. Deficient mismatch repair system in patients with sporadic advanced colorectal cancer. Br J Cancer 2009;100:266-73
3. Ganesh K, Stadler ZK, Cercek A, Mendelsohn RB, Shia K, Segal NH et al. Immunotherapy in colorectal cancer: rational, challenges and potential. Nat Rev Gastroenterol Hepatol 2019;16:361-75
4. Meric-Bernstam F, Larkin J, Tabernero J, Bonini C. Enhancing anti-tumor efficacy with immunotherapy combinations. The Lancet 2021;397:1010-1022
5. Le DT, Durham JN, Smith KN, Wang H, Bartlett BR, Aulakh LK et al. Mismatch repair deficiency predicts response of solid tumors to PD-1 blockade. Science 2017;357:409-413
6. Cervantes A, Adam R, Roselló S, Arnold D, Normanno N, Taïeb J et al. Metastatic colorectal cancer: ESMO clinical practice guidelines for diagnosis, treatment and followup. Annals of Oncology 2023;34:10-32
7. Cohen R, Rousseau B, Vidal K, Colle R, Diaz LA, André T. Immune checkpoint inhibition in colorectal cancer: microsatellite instability and beyond. Target Oncol 2020;15:11-24
8. Marus L, Fashoyin-Aje La, Donogue M, Yuan M, Rodriguez L, Gallagher PS et al. FDA approval summary: pembrolizumab for the treatment of tumor mutational burden-high solid tumors. Clin Cancer Res 2021;27:4685-9
9. Marabelle A, Fakih M, Lopez J, Shah M, Shapir-Frommer R, Nakagawa K et al. Association of tumor mutational burden with outcomes in patients with advanced solid tumors treated with pembrolizumab: prospective biomarker analysis of the multicohort, open-label, phase 2 KEYNOTE-158 study. Lancet Oncol 2020;21:1353-65
10. André T, Shiu KK, Kim TW, Jensen BV, Jensen LH, Punt C et al. Pembrolizumab in microsatellite-Instability-High advanced colorectal cancer. N Engl J Med 2020;283:2207-2218
11. Chalabi M, Fanchi LF, Dijkstra KK, Van den Berg JG, Aalbers AG, Sikorska K et al. Neoadjuvant Immunotherapy leads to pathological responses in MMR proficient and MMR deficient early-stage colon cancers. Nat Med 2020;26:566-576
12. Cercek A, Lumish M, Sinopoli K, Weiss K, Shia J, Lamendola-Essel M et al. PD-1 Blockade in mismatch repair-deficient, locally advanced rectal cancer. N Engl J Med 2022;286:2363-2376

13. Overman MJ, Lonardi S, Wong KYM, Lenz HJ, Gelsomino F, Aglietta M et al. durable clinical benefit with nivolumab plus ipilimumab in DNA mismatch repair-deficient/microsatellite instability-high metastatic colorectal cancer. J Clin Oncol 2018;36:773-779
14. André T, Lonardi S, Wong KYM, Lenz HJ, Gelsomino F, Aglietta A et al. Nivolumab plus low-dose ipilimumab in previously treated patients with microsatellite instability-high/mismatch repair-deficient metastatic colorectal cancer: 4-year follow-up from CheckMate142. Ann Oncol. 2022;33:1052-1060
15. Lenz HJ, van Cutsmem E, Limon ML, Wong KYM, Hendlisz A, Aglietta M et al. First-line nivolumab plus low-dose ipilimumab for microsatellite instability-high/mismatch repair-deficient metastatic colorectal cancer: the phase II CheckMate 142 study. J Clin Oncol 2022;40:161-170
16. Crisafulli G, Sartore-Bianchi A, Lazzari L, Pietrantonio F, Amatu A, Macagno M et al. Temozolomide treatment alters mismatch repair and boosts mutational burden in tumor and blood of colorectal cancer patient. Cancer Discov 2022;12:1656-1675
17. Morano F, Raimondi A, Pagani F, Lonardi S, Salvatore L, Cremolini C et al. Temozolomide followed by combination with low-dose ipilimumab and nivolumab in patients with microsatellite-stable, O6-methylguanine-DNA methyltransferase-silenced metastatic colorectal cancer: the MAYA trial. J Clin Oncol 2022;40:1562-73
18. Rousseau B, Patel M, Artz O, Vlachos G, Patel S, Hayatt O et al. Induction of a mismatch repair deficient genotype by tailored chemical mutagenesis in experimental models of cancer. Cancer Cell 2025;43:1313-1327
19. Willis JA, Reyes-Uribe L, Chang K, Lipkin SM, Vilar E. Immune activation in mismatch repair-deficient carcinogenesis: more than just mutational rate. Clin Cancer Res 2020;26:11-17
20. Sharma P, Hu-Lieskoban S, Wargo JA, Ribas A. Primary, adaptive and aquired resistance to cancer immunotherapy. Cell 2017;168:707-723
21. Cattaneo CM, Battaglia T, Urbanus J, Moravec Z, Voogd R, de Groot R et al. Identification of patient-specific CD4+ and CD8+ T cell neoantigens through HLA-unbiased genetic screens. Nature Biotech 2023; 41:783-787
22. Cattaneo CM, Dijkstra KK, Fanchi LF, Kelderman S, Kain S, van Rooij N et al. Tumor organoid-T cell coculture system. Nature Protocol 2020;15:15-39
23. Dijkstra KK, Cattaneo CM, Weeber F, Chalabi M, van de Haar J, Fanchi LF et al. Generation of tumor-reactive T cells by coculture of peripheral blood lymphocytes and tumor organoids. Cell 2018;174:1586-1598

24. Zang H, Wu W, Wang M, Zhang J, Gup C, Han G et al. Integrated peripheral blood multi-omics profiling identifies immune signatures predictive of neoadjuvant PD-1 blockade efficacy in head and neck squamous cell carcinoma. Journal of Translational Medicine 2025; 23:693.
25. Leick MB, Silva H, Scarfò I, Larson E, Choi BD, Bouffard AA et al. Non-cleavable hinge enhances avidity and expansion of CAR-T cells for acute myeloid leukemia. Cancer Cell 2022;40:494-508.
26. Pinho SS and Reis CA. Glycosylation in cancer: mechanisms and clinical implications. Nature Reviews Cancer 2015;15:540-555.
27. Pinho SS, Macauley MS and Laubli H. Tumor glyco-immunology, glyco-immune checkpoints and immunotherapy. Journal for ImmunoTherapy of Cancer 2025;13:e012391.
28. He K, Baniasad M, Kwon H, Caval T, Xu G, Lebrilla C et al. Decoding the glycoproteome: a new frontier for biomarker discovery in cancer. J Hematol Oncol 2024;17(1):12.
29. Crocker PR, Paulson JC and Varki A. Siglecs and their roles in the immune system. Nature Reviews Immunology 2007;7:255–266.
30. Greco B, Malacarne V, De Girardi F, Scotti GM, Manfredi F, Angelino E et al. Disrupting N-glycan expression on tumor cells boosts chimeric antigen receptor T cell efficacy against solid malignancies. Science Translational Medicine 2022; 14(628):eabg307
31. Li C, Lim S, Xia W, Lee H, Chan L, Kuo C et al. Glycosylation and stabilization of programmed death ligand-1 suppresses T-cell activity. Nature Communication 2016; 7:12632
32. Germano G, Lamba S, Rospo G, Barault L, Magrì A, Maione F et al. Inactivation of DNA repair triggers neoantigen generation and impair tumor growth. Nature 2017;552:116-120.
33. Mandal R, Samstein RM, Lee K, Havel JJ, Wang H, Krishna C et al. Genetic diversity of tumors with mismatch repair deficiency influences anti-PD-1 immunotherapy response. Science 2019;364:485-491
34. Vitiello PP, Rousseau B, Chila` R, Battuello P, Amodio V, Battaglieri V et al. Cisplatin and temozolomide combinatorial treatment triggers hypermutability and immune surveillance in experimental cancer models. Cancer Cell 2025;43:1296–1312
35. Lee H, Wang Y, Xia W, Chen C, Rau K, Ye L et al. Removal of N-Linked Glycosylation Enhances PD-L1 Detection and Predicts Anti-PD-1/PD-L1 Therapeutic Efficacy. Cancer Cell 2019; 36:168-178
36. Costa AF, Campos D, Reis CA, Gomes C. Targeting Glycosylation: A New Road for Cancer Drug Discovery. Trend in Cancer 2020; 6:757-766.
37. Perez-Riverol Y, Bandla C, Kundu DJ, Kamatchinathan S, Bai J, Hewapathirana S et al. The PRIDE database at 20 years: 2025 update. Nucleic Acids Research. 2025; 53:D543-D553.

Table legends

Table 1. Main clinicopathological features of the colorectal cancer patient's cohort.

Figure legends

Figure 1. MSS colorectal tumors show intrinsic resistance to T cell activity.

A) Experimental workflow of the study (created with BioRender.com).

B) Cell-surface HLA-A2 expression in patient derived organoids as determined by flow cytometry. Organoids were stimulated with 200 ng/mL IFNγ or left unstimulated. Bar graphs indicate median fluorescence intensity (MFI). Error bars represent SEM of at least two independent experiments. *p<0.05; **p <0.01; ***p<0.001; ****p<0.0001; ns p>0.05 (not shown on the graph); Ordinary one-way ANOVA, multiple comparisons.

C) Quantification of organoid induced IFNγ release in the supernatant. The background (spontaneous IFNγ production) was subtracted from the signal. Error bars represent SEM of at least two biological replicates. *p<0.05; **p <0.01; ***p<0.001; ****p<0.0001; ns p>0.05 (not shown on the graph); Ordinary one-way ANOVA, multiple comparisons.

D) Quantification of organoid-induced TNFα release (right). The background (spontaneous TNFα production) was subtracted from the signal. Error bars represent SEM of at least two biological replicates. *p<0.05; **p <0.01; ***p<0.001; ****p<0.0001; ns p>0.05 (not shown on the graph); Ordinary one-way ANOVA, multiple comparisons. On the left, representative histograms as determined by flow cytometry. Grey histogram represents unstained control.

E) Quantification of organoid-induced Granzyme-A release in the supernatant (right). The background (spontaneous Granzyme A production) was subtracted from the signal. Error bars represent SEM of at least two biological replicates. *p<0.05; **p <0.01; ***p<0.001; ****p<0.0001; ns p>0.05 (not shown on the graph); Ordinary one-way ANOVA, multiple comparisons. On the left, representative histograms as determined by flow cytometry. Grey histogram represents unstained control.

F) Quantification of organoid-induced Granzyme-B release in the supernatant (right). The background (spontaneous Granzyme B production) was subtracted from the signal. Error bars represent SEM of at least two biological replicates. *p<0.05; **p <0.01; ***p<0.001; ****p<0.0001; ns p>0.05 (not shown on the graph); Ordinary one-way ANOVA, multiple comparisons. On the left, representative histograms as determined by flow cytometry. Grey histogram represents unstained controls.

G) Representative flow cytometry plots gated on alive $CD3^+$ $CD8^+$ $mTCR^+$ T cells, tested for reactivity against the indicated patient-derived tumor organoids. Reactivity is measured as the percentage of $CD137^+$ cells within the total $mTCR^+$ T cell population.

H) Quantification of organoid-induced CD137 surface expression. The background (spontaneous CD137 expression) was subtracted from the signal. Error bars represent SEM of at least two biological

replicates. *p<0.05; **p <0.01; ***p<0.001; ****p<0.0001; ns p>0.05 (not shown on the graph); Ordinary one-way ANOVA, multiple comparisons.

I) On the left, representative pictures of the different patient-derived tumor organoids 24 hours after coculture with T cells. Organoids were loaded (right) or not (left) with the MART-1_{ELA} antigen. Organoids were labeled with FarRed prior to coculture. On the right, quantification of tumor organoid killing, based on the FarRed signal. Data are normalized to the control condition (organoids cocultured with T cells without antigen), shown as the white bar. Error bars represent SEM of at least two biological replicates. *p<0.05; **p <0.01; ***p<0.001; ****p<0.0001; ns p>0.05 (not shown on the graph); Ordinary one-way ANOVA, multiple comparisons.

J) Quantification of patient-derived tumor organoid killing based on flow cytometry. At the end of the 24 hours coculture, tumor organoids were dissociated into single cells and the number of live cells was quantified using counting beads. Data are normalized to the control condition (organoids cocultured with T cells without antigen), shown as the white bar. Error bars represent SEM of at least two biological replicates. *p<0.05; **p <0.01; ***p<0.001; ****p<0.0001; ns p>0.05 (not shown on the graph); Ordinary one-way ANOVA, multiple comparisons.

Figure 2. The tumor secretome is a key component of MSS intrinsic resistance to cancer immunotherapy.

A) Heatmap showing relative expression levels of a panel of immunomodulatory molecules in the supernatant of MSS- and MSI- PDOs. Colors represent fold changes in immunomodulatory molecule levels (red indicates upregulation, blue indicate downregulation). Columns represent individual patients. Each data point originates from at least 3 technical o biological replicates. Molecules and experimental conditions that have statistically significant abundance between MSS and MSI samples are marked. *p<0.05; **p <0.01; ns p>0.05 (not marked in the figure); Student t-test. For each molecule, we marked whether they are usually secreted by tumor cells, immune cells, or both.

B) Workflow of the experiment (created with BioRender.com).

C) Representative flow cytometry plots gated on CD8+ mTCR+ T cells, tested for reactivity against MSI tumor organoids in the presence of different conditioned media.

D) Quantification of IFNγ intracellular expression in T cells with MSI organoid, in the presence of the indicated conditioned media. The background (spontaneous IFNγ expression) was subtracted from the signal. The control condition (no conditioned media) was used as reference for normalization. Error bars represent SEM of at least two biological replicates. *p<0.05; **p <0.01; ***p<0.001; ****p<0.0001; ns p>0.05 (not shown on the graph); Ordinary one-way ANOVA, multiple comparisons.

E) Representative pictures of MSI_03 PDOs 24 hours after coculture with T cells. Organoids were loaded (bottom) or not (top) with the MART-1_{ELA} antigen. The coculture was performed in the absence of conditioned media (left, indicated in black), in the presence of different MSI PDOs-derived conditioned media (middle, indicated in purple) or in the presence of different MSS PDOs-derived conditioned media (right, indicated in blue).

F) Quantification of MSI patient-derived tumor organoid killing in the presence of the indicated conditioned media, based on flow cytometry. At the end of the 24 hours coculture, tumor organoids were dissociated into single cells and the number of live cells was quantified using counting beads. . Data are normalized to the control condition (organoids cocultured with T cells without antigen), shown as the white bar. Error bars represent SEM of at least two biological replicates. *p<0.05; **p <0.01; ***p<0.001; ****p<0.0001; ns p>0.05 (not shown on the graph); Ordinary one-way ANOVA, multiple comparisons.

Figure 3. Functional analysis of the tumor secretome.

A) Representative high-content microscopy images of MART-1_{ELA}–loaded tumor organoids (red) co-cultured with fluorescently labeled T cells (green). Total T cells are segmented and highlighted with a white mask, while T cells engaged in direct contact with tumor organoids are marked in blue. Engagement was quantified as the proportion of T cells physically interacting with tumor cells. The total number of T cells and the number of engaged T cells are indicated in each image.

B) Quantification of engaged T cells across different PDOs, all loaded with MART-1_{ELA} antigen; MSI samples are indicated in pink, MSS in blue. Error bars represent SEM of at least two biological replicates. *p<0.05; **p <0.01; ***p<0.001; ****p<0.0001; ns p>0.05 (not shown on the graph); Ordinary one-way ANOVA, multiple comparisons.

C) Quantification of T cell engagement with MART-1_{ELA}- loaded MSI_03 tumor organoids (left) or MSI_05 tumor organoids (left) cultured in the presence of different conditioned media. The control condition (no conditioned media, showed in white) was used as reference. *p<0.05; **p <0.01; ***p<0.001; ****p<0.0001; ns p>0.05 (not shown on the graph); Ordinary one-way ANOVA, multiple comparisons.

D) Analysis of T cell binding strength to patient-derived tumor organoids from MSI (pink) and MSS (blue) tumors. Two distinct tumor organoids lines were used for each group. Data from each experiment were normalized to their respective unpulsed controls (organoids without MART-1_{ELA} peptide loading). Mean ± SEM of biological replicates are shown. Binding strength is represented as the percentage of T cells remaining attached to tumor cells under increasing applied acoustic force.

E) Label-free membrane proteome quantification of MSI tumor organoids treated with MSS- or MSI-conditioned media for 24h. Hierarchical clustering analysis (heatmap) using unsupervised Euclidean distance of differentially expressed proteins between MSI-samples treated with MSS- or MSI-conditioned media (Student T-test, p-value <0.05. N=3 biological replicates). Each row in the figure represents a protein, each column represents a sample. Red, high expression; blue, low expression.
F) Annotations of proteins significantly upregulated across the different MSI tumor organoids treated with MSS-conditioned media. Reactome pathways enrichment analysis performed by the web tool EnrichR. Pathways categories and their relative average of enrichment scores (average $-\log_{10}$ p-value) were plotted as histogram. Pathway directly or indirectly linked to glycosylation are shown in black and grey, respectively.
G) Alluvial plot illustrating the relationship between significantly enriched pathways and glycosylation-related genes. Significantly enriched pathways identified via proteomic analysis and EnrichR are shown on the left. Each pathway is connected to glycosylation-related genes that were significantly altered and fall within that pathway. The flow passes through two intermediate layers: the nature of the link with glycosylation (direct vs. indirect), and the glycosylation gene functions to which the altered genes belong. Flows then converge on broader macrocategories representing the functional classification of these genes. The thickness of the streams corresponds to the relative number of genes involved, with thicker streams indicating direct links to glycosylation.
H) Left: Representative flow cytometry plots gated on live $CD3^+CD8^+$ $mTCR^+$ T cells co-cultured with the indicated patient-derived tumor organoids in the presence or absence of glycosylation inhibitors. T cell reactivity is measured as the percentage of $CD137^+$ cells within the total $mTCR^+$ T cell population. Right: Quantification of organoid-induced CD137 surface expression in T cells cultured with the indicated PDOs in the absence (solid color) or presence (striped bars) of glycosylation inhibitors. Background signal (spontaneous CD137 expression) was subtracted from the measured values. Error bars represent SEM from at least two biological replicates. ****$p < 0.0001$; ns $p > 0.05$ (not shown). Statistical significance was determined using ordinary one-way ANOVA with multiple comparisons.

Table 1. Main clinicopathological features of the colorectal cancer patient's cohort.

Patient ID	Sex	Age	Primary tumor location	Stage	Samples used for PDO generation	Biopsy/Resection	MMR status
MSS_01	F	52	Left colon	II	Primary tumor	Resection	MMRp
MSS_02	F	62	Left colon	IV	Liver metastasis	Resection	MMRp
MSS_03	M	66	Rectum	IV	Liver metastasis	Resection	MMRp
MSS_04	M	63	Left colon	III	Primary tumor	Resection	MMRp
MSS_05	M	68	Right colon	I	Primary tumor	Resection	MMRp
MSS_06	F	57	Rectum	III	Primary tumor	Resection	MMRp
MSS_07	F	77	Left colon	III	Primary tumor	Resection	MMRp
MSS_08	M	48	Left colon	III	Primary tumor	Resection	MMRp
MSS_09	M	72	Left colon	I	Primary tumor	Resection	MMRp
MSS_10	F	76	Left colon	I	Primary tumor	Resection	MMRp
MSS_11	M	47	Left colon	IV	Liver metastasis	Resection	MMRp
MSS_12	M	69	Right colon	III	Primary tumor	Resection	MMRp
MSS_13	F	50	Left colon	I	Primary tumor	Resection	MMRp
MSS_14	M	79	Left colon	I	Primary tumor	Resection	MMRp
MSS_15	M	49	Rectum	II	Primary tumor	Resection	MMRp
MSS_16	M	71	Left colon	I	Primary tumor	Resection	MMRp
MSS_17	M	70	Left colon	I	Primary tumor	Resection	MMRp
MSS_18	M	22	Left colon	III	Primary tumor	Resection	MMRp
MSS_19	F	84	Left colon	IV	Liver metastasis	Resection	MMRp
MSS_20	F	76	Rectum	III	Primary tumor	Resection	MMRp
MSS_21	M	81	Right colon	II	Primary tumor	Resection	MMRp
MSS_22	F	65	Left colon	II	Primary tumor	Resection	MMRp
MSS_23	M	62	Left colon	III	Primary tumor	Resection	MMRp
MSS_24	M	79	Left colon	II	Primary tumor	Resection	MMRp
MSS_25	M	73	Right colon	IV	Primary tumor	Resection	MMRp
MSS_26	F	71	Right colon	III	Primary tumor	Resection	MMRp
MSI_01	F	51	Right colon	IV	Lymphnode metastasis	Biopsy	MMRd
MSI_02	F	59	Right colon	III	Primary tumor	Resection	MMRd
MSI_03	F	59	Left colon	III	Primary tumor	Resection	MMRd
MSI_04	F	85	Right colon	III	Primary tumor	Resection	MMRd
MSI_05	F	77	Left colon	IV	Peritoneal metastasis	Biopsy	MMRd
MSI_06	F	68	Right colon	IV	Primary tumor	Resection	MMRd

Keys: PDO = patient derived organoid; MMR = mismatch Repair; MMRp = MMR proficient; MMRd = MMR deficient; M= Male; F = Female

Figure 1

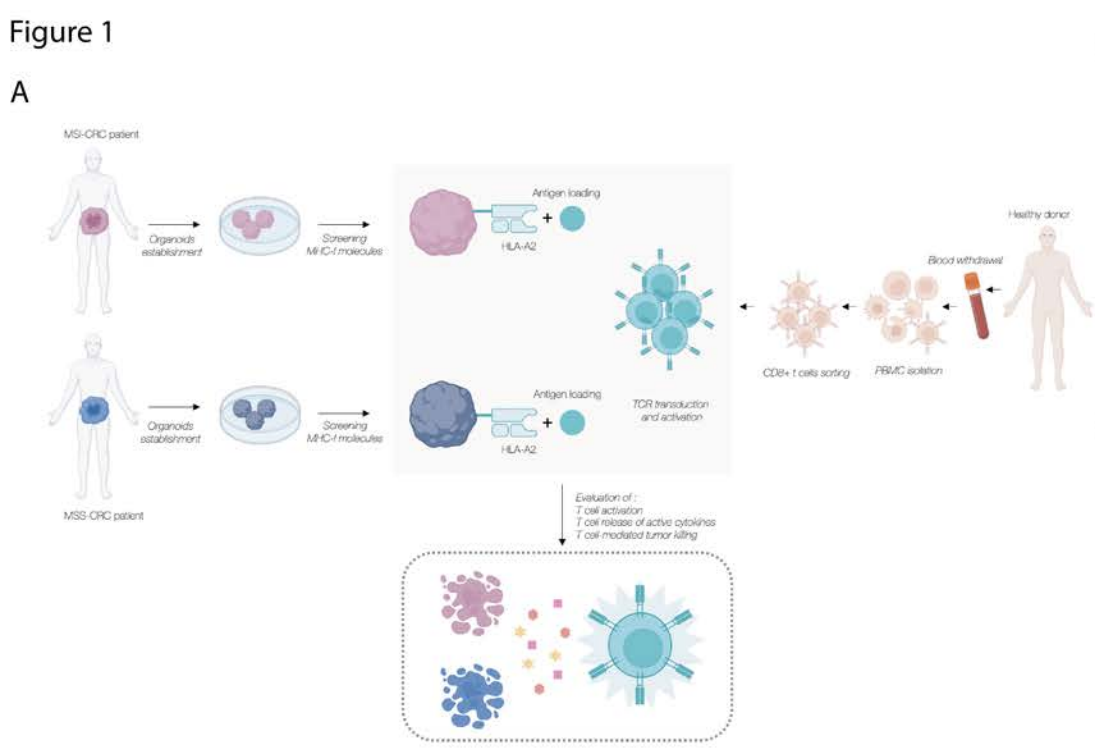

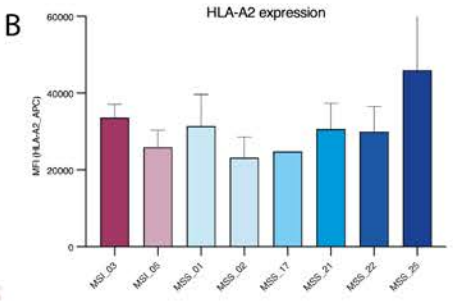

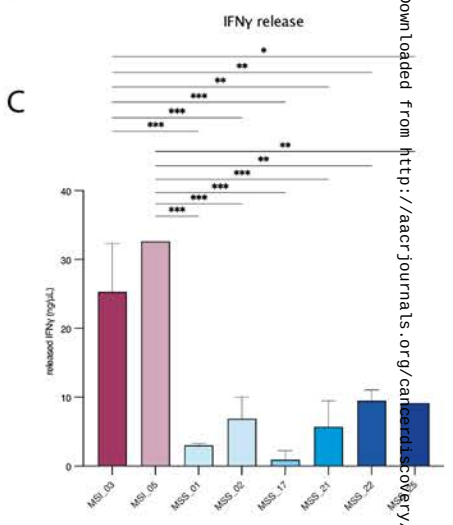

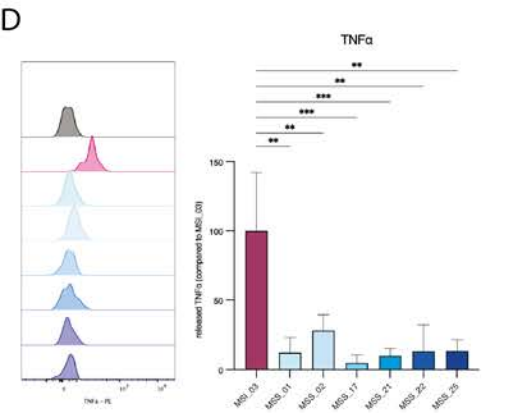

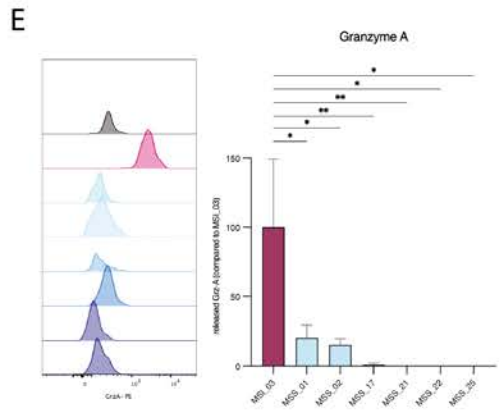

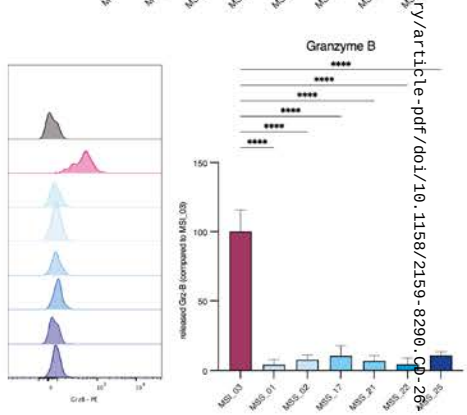

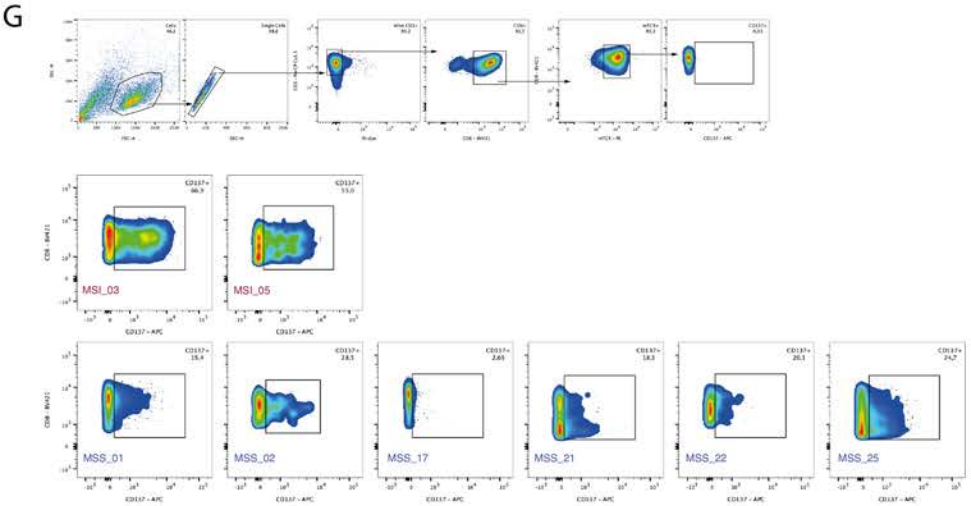

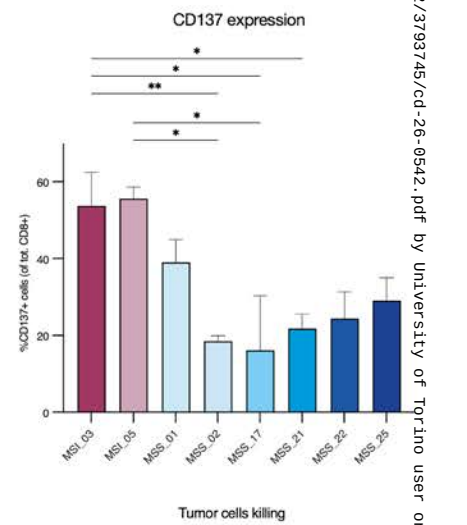

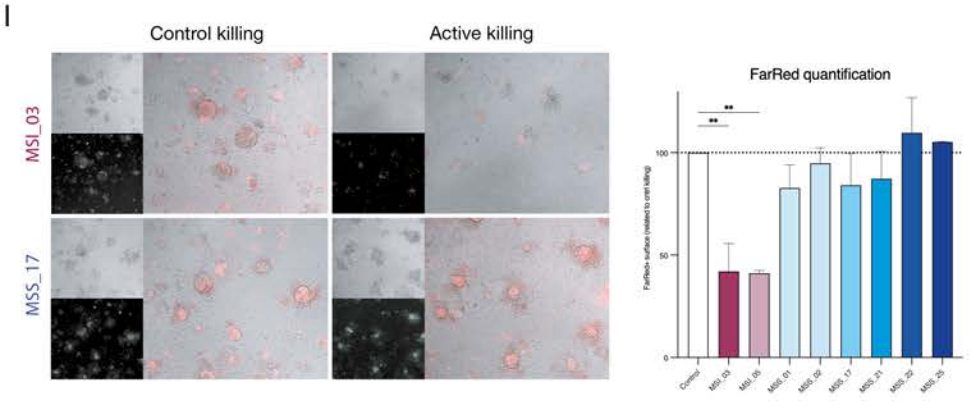

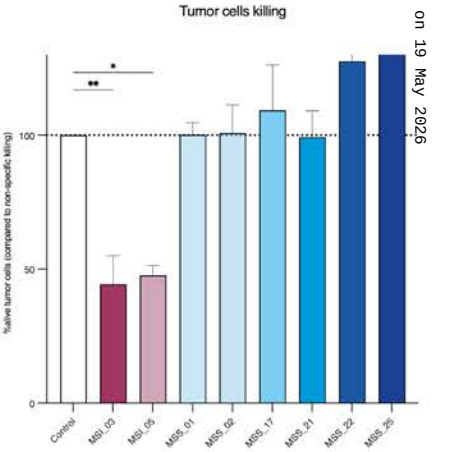

Figure 2

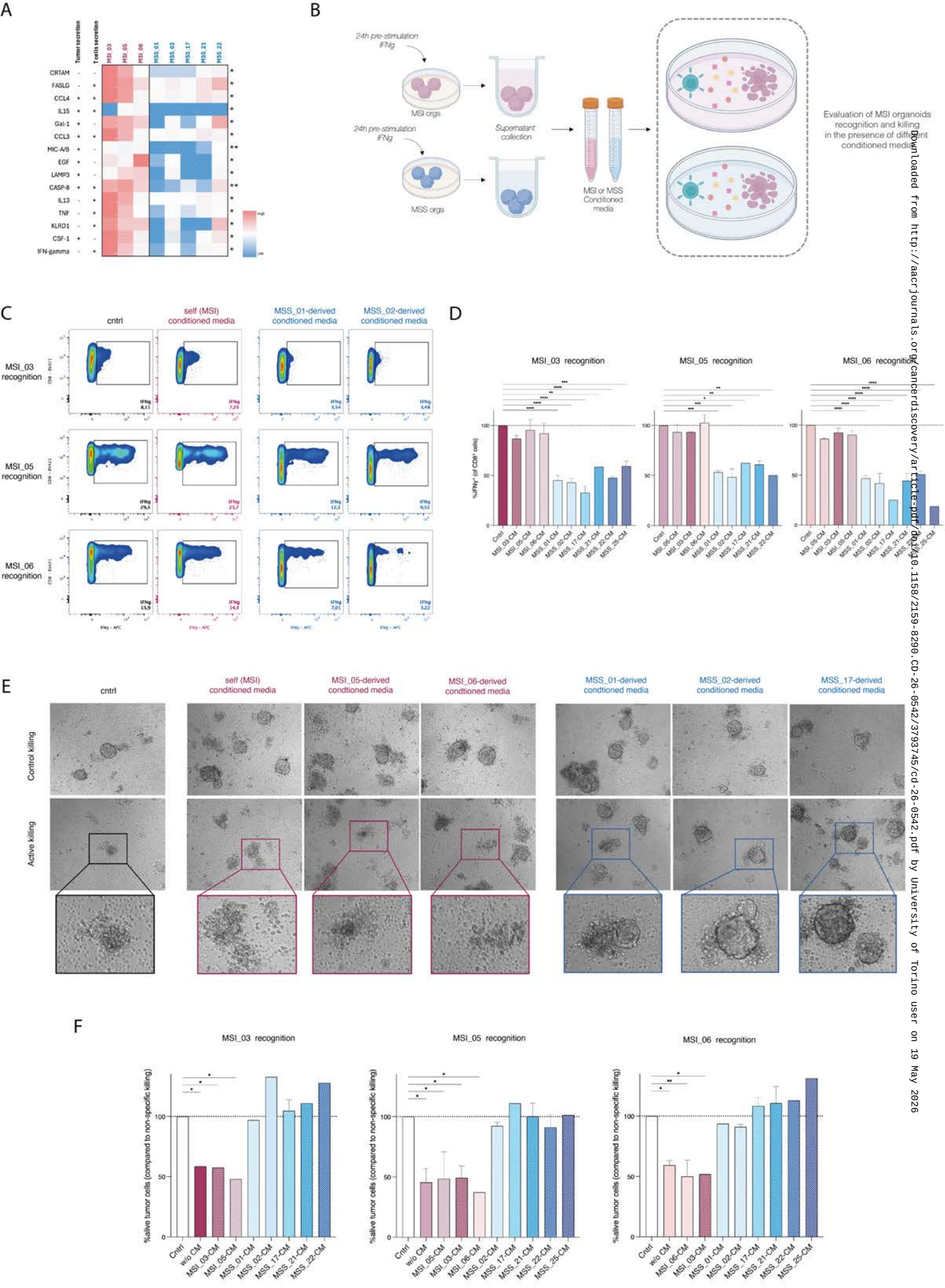

Figure 3